



1 **A case study of the large-scale traveling ionospheric disturbances in the East Asian**  
2 **sector during the 2015 St. Patrick's Day geomagnetic storm**

3  
4 Jing Liu<sup>1</sup>, Dong-He Zhang<sup>1\*</sup>, Anthea J. Coster<sup>2</sup>, Shun-Rong Zhang<sup>2</sup>, Guan-Yi Ma<sup>3</sup>, Yong-Qiang  
5 Hao<sup>1</sup>, Zuo Xiao<sup>1</sup>.

6  
7 1, Department of Geophysics, Peking University, Beijing, China, 100871

8 2, MIT Haystack Observatory, Westford, Massachusetts, USA

9 3, National Astronomical Observatories, Chinese Academy of Sciences, Beijing, China

10

11

12 **Abstract**

13 This study gives the first observation of the large-scale traveling ionospheric disturbances  
14 (LSTIDs) in the East Asian sector during the 2015 St. Patrick's Day (March 17, 2015) geomagnetic  
15 storm. For the first time, 3 dense networks of GPS receivers in China and Japan are combined  
16 together to obtain the 2-dimensional (2D) vertical total electron content (VTEC) perturbation maps  
17 in a wider longitudinal range than previous works in this region. Results show that a negative LSTID  
18 spanning at least 60° in longitude (80°E-140°E) occurs and propagating from high to lower latitudes  
19 around 09:40-11:20 UT. It is followed by a positive LSTID which shows a tendency of dissipation  
20 starting from the East side. The manifestation of the 2D VTEC perturbation maps is in good  
21 agreement with the recordings from 2 high-frequency Doppler shift stations and the iso-frequency  
22 lines from 8 ionosondes. Then, the propagation parameters of the LSTIDs are estimated by applying  
23 least square fitting methods to the distinct structures in the 2D VTEC perturbation plots. In general,  
24 the propagation parameters are observably longitudinal dependent. For example, the propagation  
25 direction is almost due southward between 105°E-115°E, while it is slightly South by West/East in  
26 the West/East side of this region. This feature is probably related to the regional geomagnetic  
27 declination. The mean values of the period, trough velocity ( $V_t$ ), crest velocity ( $V_c$ ), and wavelength  
28 of the wavelike LSTIDs in the studied longitudinal bands are  $74.8 \pm 1.4$  minutes,  $578 \pm 16$  m/s,  $617$   
29  $\pm 23$  m/s, and  $2691 \pm 80$  km, respectively. Finally, using the VTEC map data from the Madrigal  
30 database of the MIT Haystack Observatory, the characteristics of the ionospheric disturbances over  
31 the European sector (30°N-70°N, 10°E-20°E) are also studied. The results are very different from  
32 those in the East Asian sector in parameters like the occurrence time, oscillation period, and  
33 propagation velocities.

34

35

36 **Keywords: Geomagnetic Storm; LSTID; GPS TEC.**

37

38

39



## 1 1. Introduction

2 During the geomagnetic storm, the solar wind energy is impulsively or continually injected into  
3 the earth polar region and making the atmospheric and ionospheric states deviate greatly from their  
4 background levels [Fuller-Rowell et al., 1994]. In general, the response of the ionosphere to the  
5 geomagnetic storm is classified by a variety of different features, one of which is the large scale  
6 traveling ionospheric disturbance (LSTID). It is the wave-like perturbation mainly propagating  
7 equatorward from high latitudes that is considered to be the manifestation of the presence of  
8 atmospheric gravity waves (AGWs) within the ionosphere caused by Joule heating or Lorenz-drag  
9 forcing in the Auroral regions during geomagnetic storm period [Hines, 1960; Richmond and Roble,  
10 1979; Hocke and Schlegel, 1996].

11 In earlier years, the acquisition of the continuous evolution of LSTIDs on a global scale was  
12 limited by the availability of the ionospheric observations. In order to obtain the propagation  
13 characteristics of LSTIDs on a large spatial scale, researchers needed to organize their findings from  
14 limited ionospheric observations, for example, the foF2 data from sparsely distributed ionosondes.  
15 In the 1980s, the GPS method was introduced into the ionospheric study [Klobuchar, 1986; Lanyi  
16 and Roth, 1988; Coster and Gaposchkin, 1989]. With the dense and worldwide distributed GPS  
17 receivers, some characteristic ionospheric phenomena, like traveling ionospheric disturbances  
18 (TIDs) [Saito et al., 1998; Tsugawa et al., 2004; Ding et al., 2007], ionospheric storms [Ho et al.,  
19 1996], and ionospheric responses to solar flares [Afraimovich, 2000a; Zhang and Xiao, 2005] were  
20 revisited frequently and new results were obtained.

21 The propagation characteristics of LSTIDs are always topics of great research interest  
22 [Hunsucker, 1982; Ho et al., 1996; Balthazor and Moffett, 1999; Afraimovich et al., 1998, 2000;  
23 Shiokawa et al., 2002; Tsugawa et al., 2003, 2004; Ding et al., 2008, 2014; Jakowski et al., 2008;  
24 Borries et al., 2009, 2017; Habarulema et al., 2015, 2016; Zakharenkova et al., 2016; Figueiredo et  
25 al., 2017; Pederick et al., 2017; Cherniak et al., 2018; Lyons et al., 2019]. Based on limited GPS  
26 stations measurements, Afraimovich et al. [1998] propose a radio interferometry method to roughly  
27 estimate horizontal propagation velocities and phase front angles of TIDs. Further, the world-wide  
28 or local dense distribution of the GPS receivers networks facilitates the acquisition of the global or  
29 regional TEC perturbation maps with high spatial and temporal resolutions to reveal the detailed  
30 propagating characteristics of TIDs [Ho et al., 1996; Saito et al., 1998; Tsugawa et al., 2004; Borries  
31 et al., 2009; Ding et al., 2012]. With more than 60 GPS receivers distributed worldwide, Ho et al.  
32 [1996] studied the global distribution of TEC variations and perturbations during a magnetically  
33 disturbed period. They identified a TID propagating from the northern sub-auroral region to lower  
34 latitudes at a speed of about 460 m/s. The GPS Earth Observation Network (GEONET) in Japan is  
35 one of the densest GPS receiver networks on the Earth, and utilizing its data two-dimension (2D)  
36 TEC perturbations over Japan can be mapped. With these high-resolution TEC perturbation maps,  
37 the spatial structures and temporal evolutions of a TID in the nighttime mid-latitude ionosphere over  
38 Japan were revealed clearly [Saito et al., 1998]. Since then, with this dense GPS network, the  
39 characteristics of LSTIDs over Japan are carefully studied through case and statistical analysis, and  
40 some propagation features of TIDs in this region are revealed [Saito et al., 2001; Shiokawa et al.,  
41 2002; Tsugawa et al., 2003, 2004, 2006].

42 For the LSTID with scales of thousands of kilometers, the extensive spatial coverage of  
43 ionospheric observations is undoubtedly useful for capturing its propagation features. In recent years,  
44 the GPS data from densely distributed GPS stations in China are used to study LSTIDs in this region



1 [Ding et al., 2012, 2013, 2014; Song et al., 2013]. Based on the GPS data from the Crustal  
2 Movement Observation Network of China (CMONOC), Ding et al. [2012] obtains temporal  
3 continuous 2D imaging of ionospheric disturbances during the geomagnetic storm on May 28, 2011,  
4 and find two LSTIDs moving southwestward with the front width of at least 1600 km during  
5 different storm phases. In addition, through the comparative climatological study of LSTID over  
6 North America and China, the different time dependence of LSTID occurrence over two  
7 longitudinal sectors were revealed statistically [Ding et al., 2014]. These studies further emphasize  
8 the effectiveness of the large coverage, high-resolution ionospheric observations from GPS  
9 networks on the detailed investigation of the ionospheric disturbances structures.

10 The propagating direction of the LSTID during the geomagnetic storm has always been focused  
11 on for the LSTID studies. From case and statistical studies about LSTID during geomagnetic storm  
12 period over East-Asia region conducted independently by Chinese and Japanese scientists in recent  
13 years, the dominant propagating direction of LSTID in China and Japan is a little different. It mainly  
14 propagates South by West in China region [Ding et al., 2014], while it mainly propagates South by  
15 East in Japan region [Tsugawa et al., 2004]. Although the geomagnetic declination is considered to  
16 be one of the main factors to be responsible for the propagating direction of LSTID based on  
17 different LSTID studies, the LSTID studies concerning the same geomagnetic storm using both  
18 China and Japan GPS networks together have not yet been reported.

19 During the period of 17–18, March 2015, a large geomagnetic storm occurred, which is the  
20 strongest one in the 24th solar cycle. During this storm, LSTIDs over European and American  
21 sectors are detected and analyzed with data from Global Navigation Satellite Systems (GNSS)  
22 stations [Zakharenkova et al., 2016]. Meanwhile, two high frequency (HF) Doppler stations  
23 operated by China Meridional Project [Wang, 2010] at mid-latitude China record a large ionospheric  
24 HF Doppler shift after 10:00 UT, which appears to indicate LSTIDs related to the geomagnetic  
25 storm. In this study, the multi-network of densely distributed GPS receivers and an ionosonde  
26 network will be used to reveal the propagating characteristics of these large disturbances recorded  
27 in HF Doppler shift receivers in the East Asian region, especially the characteristics of the dominant  
28 propagating direction of this disturbance over China and Japan.

29

## 30 2. Data and Methods

31 Figure 1 illustrates the locations of ground-based receivers that are used in this study from 4  
32 GNSS networks distinguished by colors. They are Chinese Meteorological GNSS Network  
33 (CMGN), CMONOC in China, GEONET in Japan, and International GNSS Service (IGS). These  
34 receivers are selected through data quality checking and regional restriction ( $10^{\circ}\text{N} \sim 60^{\circ}\text{N}$ ,  $70^{\circ}\text{E} \sim$   
35  $150^{\circ}\text{E}$ ), and the numbers of used stations are 259, 220, 1300, and 31 for CMGN, CMONOC,  
36 GEONET, and IGS, respectively. The sample rate of all GPS data is 30 seconds. Combining the  
37 carrier phase and pseudo-range measurements in two L-band frequencies of GPS receivers'  
38 observations, the vertical TEC can be obtained. In the calculation, the height of the ionospheric thin  
39 shell is set to be 400 km, and the cutoff elevation angle is 30 degrees. The detailed process of the  
40 TEC calculation from GPS data can be found in our previous works [Zhang et al., 2009; Zhang et  
41 al., 2010].

42 Different methods have been used for extracting the TEC perturbations related to LSTIDs in  
43 previous works [Wan et al., 1997; Afraimovich et al., 2000; Shiokawa et al., 2002; Nicolls et al.,  
44 2004; Tsugawa et al., 2004; Ding et al., 2007]. Afraimovich et al. [2000] suggest that the LSTID



1 characteristics in TEC can be determined by removing the trend with 3 to 5 order polynomials in  
2 order to eliminate the trends introduced by the motion of satellites and variations of the regular  
3 ionosphere. For a similar purpose, Shiokawa et al. [2002] subtract a running average of TEC over 1  
4 hour from the raw TEC. With more than 1000 GPS receivers over Japan, a series of 2D TEC  
5 perturbation maps can be obtained. Ding et al. [2007] develop another method of obtaining the 2D  
6 TEC perturbation maps by expressing the vertical TEC as a one-order function of local time and  
7 latitude. According to their argument, this method is sufficient to remove background trends for  
8 continuous observation of a GPS receiver-satellite pair without introducing artificial perturbations.  
9 After comparing the results of these methods, a method similar to Ding et al. [2007] is conducted in  
10 this study, in which the vertical TEC at an ionospheric pierce point (IPP) is treated as a function of  
11 universal time (UT), longitude (Lon), and latitude (Lat), i.e.,

$$12 \quad VTEC_0 = C_0 + C_1 UT + C_2 Lon + C_3 Lat$$
$$13 \quad VTECP = VTEC - VTEC_0$$

14 in which  $VTEC_0$  is the background change and  $VTECP$  is VTEC perturbation. Then, the obtained  
15  $VTECP$  data is reorganized into pixels which are bounded by  $10^\circ N \sim 60^\circ N$ ,  $70^\circ E \sim 150^\circ E$  and with  
16 a spatiotemporal resolution of  $1^\circ$  longitude  $\times$   $1^\circ$  latitude  $\times$  10 minutes. The  $VTECP$  value for each  
17 pixel is set to be the average of all  $VTECP$  data of which the IPP and UT locate in this pixel. After  
18 these steps, the featured ionospheric disturbances are expected to appear on a series of 2D  $VTECP$   
19 maps.

20 As a comparison, the VTEC map from Madrigal database of the MIT Haystack Observatory  
21 (<http://cedar.openmadrigal.org/>) is used to reveal the ionospheric disturbances in the European  
22 sector ( $30^\circ N \sim 70^\circ N$ ,  $10^\circ E \sim 20^\circ E$ ). This database provides worldwide VTEC values in  $1^\circ$  latitude  
23  $\times$   $1^\circ$  longitude pixels with a temporal resolution of 5 minutes [Rideout and Coster, 2006] and has  
24 good data coverage in European and American sectors. VTEC maps with such a high spatiotemporal  
25 resolution are suitable to reveal the structures of traveling ionospheric disturbances [Zhang et al.,  
26 2017].

27 The Doppler shift data observed at two high frequency (HF) Doppler sounding stations in  
28 China is collected, of which the station codes are MDT ( $40.4^\circ N$ ,  $116.9^\circ E$ ), and SZT ( $22.6^\circ N$ ,  
29  $114.1^\circ E$ ). The sounding system continuously receives electromagnetic waves with a stabilized  
30 frequency of 10 MHz transmitted by the National Time Service Center (NTSC) ( $35.7^\circ N$ ,  $109.6^\circ E$ )  
31 to detect the ionospheric disturbances through the Doppler shifts of this standard frequency. These  
32 shifts are considered to be caused by ionospheric variations mainly around the reflecting point of  
33 the electromagnetic wave in the ionosphere. According to the geometrical relationships, the  
34 locations of the reflecting point for MDT and SZT are ( $38.0^\circ N$ ,  $113.2^\circ E$ ) and ( $29.2^\circ N$ ,  $111.8^\circ E$ ),  
35 respectively. These stations are marked in Figure 1 with colored stars.

36 In this study, ionograms from 8 ionosonde stations in China middle latitude are used to derive  
37 the iso-frequency lines, which vary as a function of universal time and virtual height. The sample  
38 rate of the ionograms is 15 minutes. These ionosondes belong to the China Research Institute of  
39 Radio-wave Propagation (CRIRP) and their locations are marked in Figure 1 with lime triangles. In  
40 addition, the condition of the geomagnetic storm is shown with data from the high resolution (5  
41 minutes) OMNI dataset, which is downloaded from the FTP service of the NASA Goddard Space  
42 Flight Center (<https://spdf.gsfc.nasa.gov>).

43

### 44 3. Results



### 1 3.1 Observations

2 Figure 2 shows the variations of (a) solar wind speed, (b) interplanetary magnetic field (IMF)  
3  $B_z$  component, (c) the SYM-H index, and (d) the AE index from the OMNI dataset, and the time  
4 range is from 18:00 UT, 16 March 2015 to 06:00 UT, 18 March 2015. It should be noted that the  
5 solar wind magnetic field and plasma data are time-shifted to the bow shock nose to better support  
6 the solar wind-magnetosphere coupling studies. It can be seen clearly that a geomagnetic storm  
7 occurred on 17 March 2015, with the sudden storm commencement (SSC) at  $\sim 04:45$  UT, which is  
8 characterized by a sharp increase (marked with vertical dashed lines) in the solar wind speed,  $B_z$ ,  
9 and SYM-H index. The main phase of the storm can be roughly divided into two stages. The first  
10 stage is from  $\sim 06:00$  UT, when the IMF  $B_z$  component first turns to southward, to  $\sim 12:00$  UT,  
11 when the  $B_z$  turns southward again after back to northward for about 2 hours. After  $\sim 12:00$  UT, the  
12  $B_z$  is southward for the most time, until it enters the recovery phase. The SYM-H and AE indices  
13 show a similar two-stage feature as the  $B_z$ . The SYM-H decreases after  $\sim 06:00$  UT, reaches the  
14 first minimum at  $\sim 09:30$  UT, and increases to a local maximum at  $\sim 12:00$  UT. Then, it gradually  
15 decreases with small oscillations and reaches the minimum value of  $-233$  nT at  $\sim 22:45$  UT.  
16 Correspondingly, the AE index exhibits the first increase period between 06:00 UT to 12:00 UT,  
17 with the maximum intensity of  $\sim 1000$  nT, and the second period between 12:00 UT to 02:00 UT of  
18 the next day, during which the AE increases much larger with several peaks. This storm is the  
19 strongest one in the 24th solar cycle [Astafyeva et al., 2015].

20 During the first stage of the main phase, disturbances are observed successively at two HF  
21 Doppler receiver stations shown in Figure 1. Figure 3 illustrates the variations of the Doppler shift  
22 records at (a) MDT and (b) SZT between 08:00 UT and 14:00 UT on 17 March 2015. It shows that  
23 two distinct positive shifts occur at about 10:21 UT and 10:55 UT, respectively. Shortly after, it  
24 exhibits two negative shifts but with much smaller amplitudes. Suppose these successive  
25 disturbances indicate a propagating perturbation, according to the estimated locations of the  
26 reflecting points that mention above and the occurrence time of the two positive peaks, the  
27 approximate speed of this perturbation is about 553 m/s. This value is much larger than the speed  
28 of the movement of the ionospheric negative storm that usually occurs in the middle latitude due to  
29 storm-induced equatorward wind [Buonsanto, 1999], and the ionospheric storm is not serious in the  
30 Asian sector during this period [Astafyeva et al., 2015]. Considering the propagating speed and the  
31 interval of the positive-negative variations, the recorded perturbations probably reflect an  
32 equatorward propagating LSTID in the East Asian sector.

33 To confirm this, Figure 4 presents a sequence of 2D VTECP maps between 09:40-11:40 UT on  
34 17 March 2015 with the method described above. The grey areas represent the night side. Note that  
35 the raw value of VTECP is converted into VTECP' with

$$36 \quad VTECP' = \text{sign}(VTECP) * \log_{10}(\text{abs}(VTECP) + 1)$$

37 to make it easier to distinguish the regions with positive and negative perturbations. The yellow  
38 lines illustrate the least square fitting results for all the negative pixels within certain rectangular  
39 areas bounded by longitudes and latitudes. The lime lines are similar but for pixels with values close  
40 to zero (see below for example). These two kinds of lines mark the approximate locations of the  
41 wavefronts.

42 A large-scale wavelike perturbation can be seen clearly in Figure 4. The first relatively distinct  
43 wave structure emerges during the (d) 10:10-10:20 UT period, while its sign can already be observed  
44 as early as (a) 09:40-09:50 UT in the northwest part of China. During (e) 10:20-10:30 UT, a negative



1 band that across both China and Japan sectors occur between around 30°N-45°N, which gradually  
2 propagates to lower latitudes in the next tens of minutes. During (f) 10:30-1040 UT, the first clear  
3 wavefront of the positive band appears, which also shows an equatorward movement for at least  
4 half an hour. Finally, there seems to be no distinct wave structure following the positive band.  
5 Considering the spatiotemporal characteristics of this perturbation, it can be preliminarily identified  
6 as an LSTID. By the way, it is interesting to note that the positive bands do not extend to the Japan  
7 sector in (h) and (i), and the corresponding VTECP' amplitudes seem smaller in the East side than  
8 in the West side. This may be probably related to that the Japan sector has already entered the  
9 nightside.

10 Both the negative and positive bands exhibit more complex variations when they enter the  
11 equatorial ionospheric anomaly (EIA) region between 20°N-30°N. On the one hand, the amplitude  
12 of VTECP' is relatively larger than those in the higher latitudes. On the other hand, it seems that  
13 the equatorward propagating of the negative band decelerates significantly in this area, which is  
14 especially shown in (g-l). Such complex features are probably related to the various physical  
15 processes in this region. Ding et al. [2012] suggest that LSTIDs experience severe dissipation in  
16 South China region due to viscosity and heat conductivity at low latitudes, which may account for  
17 the weakening of the equatorward propagating of the wavelike structures.

18 Our observations of the Doppler shift and VTECP' maps are in good agreement. To show it  
19 clearly, Figure 5 shows the variations of the mean VTECP' data near the Doppler reflection points  
20 with the same time range of Figure 3. It can be seen that the troughs at around 10:20 UT in (a) and  
21 10:50 UT in (b) correspond well to the two distinct crests in Figure 3. In addition, the variations of  
22 the VTECP' between 11:00 and 14:00 are also in a good negative correlation with the Doppler shift  
23 observations for each reflecting point. It should be noted that the variation of VTECP' at the  
24 reflecting point 1 exhibits more variability than that at the reflecting point 0, especially around 09:00  
25 UT, 10:00 UT, and 12:00 UT. Considering that point 1 (29.2°N, 111.8°E) is approaching the EIA  
26 region, the causes for VTEC perturbations are more complicated as mentioned above. This feature  
27 is consistent with the observations of the 2D VTECP' maps in Figure 4.

28 Ionospheric parameters from ionograms have been commonly used since early TID studies.  
29 Recently, ionograms observed by digital ionosondes with a sampling rate as high as 100 seconds  
30 was used in TID studies [Klausner et al, 2009]. Figure 6 presents the temporal variations of the  
31 virtual height for iso-frequency lines from ionograms. The names and locations of the corresponding  
32 ionosondes are given in each subplot. On the left side, the results of five stations are arranged in  
33 order from high to lower latitudes, and on the right side, it shows the recordings of four stations in  
34 the same latitudinal belt. The corresponding frequencies are also marked for each iso-frequency line.  
35 We can see clearly that a distinct uplift of the virtual height occurs at 09:45 UT at Manzhouli station,  
36 and it gradually moves equatorward from high to lower latitudes (a-e). Meanwhile, the phase  
37 difference is not observed for the stations on the right column. This means that the ionospheric  
38 disturbance roughly moves along the meridian line in this longitudinal sector (around 115°E), which  
39 corresponds to the results of the 2D VTECP' map. Moreover, although the time resolution of 15  
40 minutes is relatively low, it can still be identified that the crests in the higher iso-frequency lines  
41 appear earlier than those in the lower ones. Such trends (marked with red dashed lines) indicate a  
42 downward vertical phase velocity, which is one of the typical characteristics of TID and AGW [Hine,  
43 1960; Hocke and Schlegel, 1996].

44



### 1 3.2 Estimating Propagation Parameters

2 As preparation for estimating the propagating parameters of this LSTID, Figure 7 shows a  
3 detailed example of the wavefront fitting method with the VTECP' map in Figure 4(g) (10:40-10:50  
4 UT). The reason for choosing this period is that the structure of the wavefront is relatively clear, and  
5 the boundary of the positive and negative wave band in the Japan sector can still be partly identified.  
6 The lime line is the least square fitting for the lime dots, of which the absolute VTECP' values are  
7 small enough (bottom 5%) among all the dots in a certain region (75°E-140°E, 30°N-40°N). The  
8 wave propagating azimuth (marked with arrows) can be estimated with the normal direction of this  
9 fitting line. Results are listed in Table 1 in the second column.

10 It can be seen clearly that the TID moves due South around 110°E, and in the West/East region,  
11 the propagation direction is slightly South by West/East. It should be noted that the morphology of  
12 this TID is continuously changing as it moves from high to lower latitudes. Although the azimuths  
13 are estimated only with the wavefront data during 10:40-10:50 UT, such longitudinal dependence  
14 of azimuths corresponds well with other fitting lines in Figure 4(e, f, g, h).

15 In order to derive the phase speed, period, and wavelength of this LSTID, the time-latitude  
16 plots (TLPs) of VTECP' are obtained for six longitudinal bands, which are marked with dashed  
17 rectangles in Figure 7. For each band, the VTECP' data is averaged along the latitude for every 6  
18 minutes (0.1 hours), and the results as a function of UT and latitude are illustrated in Figure 8. As  
19 mentioned before, the variation of VTECP' in the EIA region is rather complex, so only the values  
20 over 30°N (marked with dashed lines) are used to estimate the speed.

21 As expected, the most distinctive structures in all panels are the pair of negative and positive  
22 bands around 10:40 UT, which correspond to the perturbations moving from high to lower latitudes  
23 shown in Figure 4. The structures in the 130°E-140°E are not quite clear, which may be due to the  
24 lack of data in some parts of this area, but the trough around 10:40 UT can still be identified. To  
25 estimate the meridional phase speeds of these perturbation patterns, the linear least square method  
26 is used to fit the pairs of troughs and crests. The data points for the linear fitting are marked with  
27 white dots, which are the minimum/maximum values along with each latitudinal bin around the  
28 negative/positive structures that we focus on. The phase speeds for wave troughs ( $V_t$ ) and crests  
29 ( $V_c$ ) can be derived based on the slopes of the fitting lines. Moreover, the period of the wave can  
30 be estimated through the time interval between the trough and crest in TLPs. In practice, for each  
31 longitudinal region, the average of time lags along all latitudinal bins is set to be the half period of  
32 the wave in this region. Finally, with the period and speed, the wavelength can be easily determined.

33 However, those speed, period, and wavelength are the projections on longitudes. After adjusted  
34 by the propagation azimuths that calculated above, the final results of the estimated parameters are  
35 also listed in Table 1. The longitudinal dependence of these parameters can be seen clearly. The  
36 mean values and standard deviations of the period,  $V_t$ ,  $V_c$ , and wavelength are  $74.8 \pm 1.4$  minutes,  
37  $578 \pm 16$  m/s,  $617 \pm 23$  m/s, and  $2691 \pm 80$  km, respectively. It shows that  $V_t$  is in good agreement  
38 with the result of 553 m/s derived from the Doppler observation. These parameters are typical for  
39 an LSTID. Besides, it is interesting to note that the mean  $V_c$  is slightly larger than the mean  $V_t$ ,  
40 which seems like the wave behind is pushing that ahead.

41 As mentioned above, the VTECP' in the EIA region seems to exhibit different features  
42 compared to that in the middle latitude. It can be seen from Figure 8(c) that VTECP' in this region  
43 also shows a periodic variation, but its period seems larger and time duration is longer than the  
44 LSTID. These disturbances are probably related to the complex variations of VTEC after 08:00 UT



1 (around dusk). Besides, the perturbations at 20°N around 12:00 UT and 13:00 UT show patterns of  
2 poleward movement. Ding et al. [2013] have studied the poleward-propagating LSTIDs in southern  
3 China during a medium-scale storm in 2011. They attribute their observations to the excitation of  
4 secondary LSTIDs during the dissipation of primary disturbances from the lower atmosphere. In  
5 addition, the poleward-moving disturbances may also be induced by the variation of the equatorial  
6 electrojet [Chimonas, 1970] or just propagate from the southern hemisphere [Zakharenkova et al.,  
7 2016]. A detailed investigation of this phenomenon is not the focus of this work.

8

#### 9 4. Discussion

10 Our results show that the propagation parameters of the LSTID in the East Asian sector during  
11 the St. Patrick's Day storm are longitudinal dependent. Among these parameters, the longitudinal  
12 dependence of the propagation azimuth of an LSTID receives much attention in previous works. In  
13 general, earlier studies suggest that there are four main factors that affect the direction of a polar  
14 originated LSTID, which are the velocity of the background neutral wind [Hines, 1960; Morton and  
15 Essex, 1978; Maeda and Handa, 1980], the structure and evolution of the source region in the auroral  
16 oval [Maeda and Handa, 1980; Hunsucker, 1982; Ding et al., 2007], the Coriolis force [Maeda and  
17 Handa, 1980; Balthazor and Moffett, 1999; Afraimovich et al., 2000; Tsugawa et al., 2004; Ding et  
18 al., 2013], and the declination of geomagnetic field [Tsugawa et al., 2004; Jakowski et al., 2008;  
19 Borries et al., 2009].

20 The Coriolis force effect is generally believed to contribute to the clockwise shift of the  
21 propagation direction of the LSTIDs [Afraimovich et al., 2000; Tsugawa et al., 2004; Ding et al.,  
22 2013]. The observations of the shift (10°-20° on average) are consistent with the calculation by Maeda  
23 and Handa [1980] and the model simulation by Balthazor and Moffett [1999]. However, in our study,  
24 the shift of the propagation direction is not systematic westward, which means the variability of the  
25 LSTID azimuth in our observation cannot be attributed to the Coriolis force, at least not to it alone.

26 The structure/movement of the source region for the LSTID in the auroral oval is another  
27 candidate for explaining the longitudinal dependence of the propagation direction of the LSTID.  
28 Previous studies have suggested that the westward movement of enhanced electrojets in the auroral  
29 arc is an important cause of the westward shift of the LSTID propagation direction at high latitudes  
30 [Hunsucker, 1982; Ding et al., 2007]. The change of the propagation direction of LSTIDs as they  
31 move from high to middle latitudes during the superstorm of 29 October 2003 over North America,  
32 was explained by Ding et al. [2007] as related to a change in the position of the electrojet  
33 enhancement area near the auroral oval. Nevertheless, since the structure and the evolution process  
34 of the source region during storm period is complicated, more cases and modeling studies are needed  
35 to find a clear connection between it and the propagation direction of LSTIDs.

36 In general, the velocity of the neutral wind is much less than that of the LSTIDs, and the  
37 thermospheric wind velocity in the same latitudinal belt with a limited longitudinal extension should  
38 exhibit little variance. So the contribution of the background wind on the change of the propagating  
39 direction would be limited in the absence of the geomagnetic field. However, a combined effect of  
40 magnetic declination and zonal wind can cause F region electron density differences between two  
41 sides of the zero declination [Zhang et al., 2011]. During storm periods, the enhanced zonal winds  
42 [Fuller-Rowell et al., 1994] can intensify these differences [Thomas et al., 2016]. As a result, the  
43 geomagnetic declination is considered to be an important factor that affects the propagation  
44 direction of the LSTID. Some researchers have studied the predominant propagation direction of





1 LSTIDs during storm periods in different longitudinal sectors, and suggest that, statistically  
2 speaking, the predominant directions of LSTID in European continent, China and Japan are  
3 primarily southward, South to West and South to East, respectively [Nicolls et al, 2004; Tsugawa et  
4 al, 2004; Jakowski et al, 2008; Borries 2009; Ding et al, 2013]. These results are all consistent with  
5 the corresponding geomagnetic declination in each sector.

6 In the longitudinal region of 70°E-150°E, the geomagnetic declination angles change from  
7 North by East in the West side to North by West in the East side. This characteristic seems to show  
8 some kind of consistent with the azimuth results in Table 1. To illustrate such connection  
9 quantitatively, Figure 9 depicts the (a) the geomagnetic declination on the wavefront in different  
10 longitudes in Figure 7 and (b) the propagation direction (azimuth-180°) of the LSTID at the same  
11 spot. The connection between these two parameters is quite obvious in this event. This result  
12 manifests that the propagation of LSTIDs in different longitudes is probably influenced by the  
13 orientation of the geomagnetic field lines in the East Asian sector. In addition, the tendency of field-  
14 aligned propagation of the LSTID indicates that it is driven by the neutral winds rather than by  
15 electric fields since the winds push the plasma up and down along the magnetic field lines. It should  
16 be noted that our speculation needs to be verified with more observational data and numerical  
17 simulation to reduce uncertainty in our propagation estimation and to figure out the detailed physical  
18 processes.

19 Zakharenkova et al. [2016] have studied the behaviors of LSTIDs during the St. Patrick's Day  
20 storm for the European and American sectors with GPS and GLONASS observations. It shows  
21 clearly in their results that the European sector (10°E) also exhibits LSTIDs around 11:00 UT. As a  
22 comparison, these LSTIDs are also investigated but with VTEC data from the Madrigal database of  
23 the MIT Haystack Observatory. This database has good spatiotemporal coverage for the European  
24 and American sectors. To derive the VTECP, a narrow longitudinal band (10°E-20°E, 30°N-70°N)  
25 is first selected and the VTEC data with the same latitude at the same time is average. At each  
26 latitude bin, the averaged VTEC forms a time series and the temporal resolution is reset to 12  
27 minutes (0.2 hours) with bin averaging. Then, a running mean with a 1.5 hours window is conducted  
28 for each time series and their difference is taken as the VTECP. The result is plotted in Figure 10 as  
29 a TLP. The fitting lines are obtained with a similar method mentioned above.

30 Figure 10 is basically consistent with the Figure 3(b) in Zakharenkova et al. [2016], such as the  
31 synchronous perturbations around 04:45 UT and 09:15 UT, and the LSTID structures between 10:00  
32 UT and 17:00 UT. Moreover, our result shows that the VTECP' behavior between 60°N and 70°N  
33 is quite different from below. The pattern around 10:00 UT seems to represent a TID with smaller  
34 phase speed. Considering the physical processes are more complex in such high latitudes [Foster et  
35 al., 2014], we only focus on the perturbations below 60°N. The phase speeds estimated from the  
36 crest and trough are  $\sim 500 \pm 51$  m/s and  $\sim 427 \pm 55$  m/s, respectively, and the estimated period is  $\sim$   
37  $4.0 \pm 0.2$  hours. It is clear that the appearances of the LSTIDs are different in the European and the  
38 East Asian sectors during the same UT period for the same storm event. This may be related to the  
39 location or structure of the Joule heating source in the auroral oval or the difference of the  
40 background TEC in the two sectors. For better understanding this difference, more studies on the  
41 Joule heating source are needed.

42

43

44 **5. Summary**



1 Using data from 4 GPS receiver networks (CMGN, CMONOC, GEONET, IGS), together with  
2 recordings of 2 HF Doppler shift stations and 8 ionosondes, we show the first observation results of  
3 the LSTIDs in the East Asian sector during the 2015 St. Patrick's Day storm. The GPS receiver  
4 networks in China and Japan are combined together to produce 2D VTEC perturbation maps in  
5 order to give a wider image of the LSTID structures in the East Asia. As a comparison, the  
6 ionospheric disturbances in the European sector are also studied with VTEC data from the Madrigal  
7 database. The propagation parameters of the LSTIDs are estimated. Main results can be summarized  
8 as follows:

9 (1) A negative LSTID occurs and propagates from high to lower latitudes during 09:40-11:20  
10 UT, which spans over  $60^\circ$  in longitude. It is followed by a positive LSTID characterized by a clear  
11 tendency to dissipate which starts from the East side. These features are in good agreement with  
12 observations by HF Doppler shift stations and ionosondes

13 (2) The propagation orientation is almost due southward around  $105^\circ\text{E}$ - $115^\circ\text{E}$ , and it tends to  
14 slightly shift westward/eastward in the West/East part of the studied area. This may be influenced  
15 by the regional declination of the geomagnetic field lines.

16 (3) Other propagation parameters are also longitudinal dependent (see Table 1), and the mean  
17 values and standard deviations of the period,  $V_t$ ,  $V_c$ , and wavelength are  $74.8 \pm 1.4$  minutes,  $578 \pm$   
18  $16$  m/s,  $617 \pm 23$  m/s, and  $2691 \pm 80$  km, respectively.

#### 19 20 **Acknowledgement:**

21 We are grateful to the International GPS Services (IGS) (<ftp://cddis.gsfc.nasa.gov>). The GPS data  
22 from CMONOC and CMGN networks are provided by the China Earthquake Administration (CEA)  
23 and the China Meteorological Administration (CMA), respectively. The GPS data from GEONET  
24 are provided by the Geographical Survey Institute, Japan. GPS TEC data products and access  
25 through the Madrigal distributed data system are provided to the community by the Massachusetts  
26 Institute of Technology under support from the US National Science Foundation grant AGS-  
27 1242204. The HF Doppler records are from the Chinese Meridian Project. The ionosonde data are  
28 provided by the China Research Institute of Radio wave Propagation (CRIRP). We thank the  
29 NASA/GSFC's Space Physics Data Facility's OMNIWeb service for data of the interplanetary and  
30 SYM-H parameters. This research was supported by the National Natural Science Foundation of  
31 China (No. 41674157).

#### 32 33 34 **References**

- 35 Afraimovich, E. L., Palamartchouk, K. S., and Perevalova, N. P.: GPS radio interferometry of  
36 travelling ionospheric disturbances. *Journal of Atmospheric and Solar-Terrestrial*  
37 *Physics*, 60(12), 1205-1223, 1998.
- 38 Afraimovich, E. L., Kosogorov, E. A., Leonovich, L. A., Palamartchouk, K. S., Perevalova, N. P.,  
39 and Pirog, O. M.: Determining parameters of large-scale traveling ionospheric disturbances of  
40 auroral origin using GPS-arrays. *Journal of Atmospheric and Solar-Terrestrial Physics*, 62(7),  
41 553-565, 2000.
- 42 Astafyeva, E., Zakharenkova, I., and Förster, M.: Ionospheric response to the 2015 St. Patrick's Day  
43 storm: A global multi-instrumental overview. *Journal of Geophysical Research: Space*  
44 *Physics*, 120(10), 9023-9037, 2015.



- 1 Balthazor, R. L. and Moffett, R. J.: Morphology of large-scale traveling atmospheric disturbances  
2 in the polar thermosphere. *Journal of Geophysical Research: Space Physics*, 104(A1), 15-  
3 24. Borries, C., Jakowski, N., & Wilken, V. (2009). Storm induced large scale TIDs observed  
4 in GPS derived TEC. *Ann. Geophys.*, 27(4), 1605-1612, 1999.
- 5 Borries, C., Jakowski, N., Kauristie, K., Amm, O., Mielich, J., and Kouba, D.: On the dynamics of  
6 large-scale traveling ionospheric disturbances over Europe on 20 November 2003. *Journal of*  
7 *Geophysical Research: Space Physics*, 122(1), 1199-1211, 2017.
- 8 Buonsanto, M. J.: Ionospheric storms—A review. *Space Science Reviews*, 88(3-4), 563-601, 1999.
- 9 Cherniak, I. and Zakharenkova, I.: Large-Scale Traveling Ionospheric Disturbances Origin and  
10 Propagation: Case Study of the December 2015 Geomagnetic Storm. *Space Weather*, 16(9),  
11 1377-1395, 2018.
- 12 Chimonas, G.: The equatorial electrojet as a source of long period travelling ionospheric  
13 disturbances. *Planetary and Space Science*, 18(4), 583-589, 1970.
- 14 Coster, A. J. and Gaposchkin, E. M.: Use of GPS pseudo-range and phase data for measurement of  
15 ionospheric and tropospheric refraction. In *Institute of Navigation Satellite Division, 2nd*  
16 *International Technical Meeting* (pp. 439-443), 1989.
- 17 Ding, F., Wan, W., Ning, B., and Wang, M.: Large-scale traveling ionospheric disturbances observed  
18 by GPS total electron content during the magnetic storm of 29-30 October 2003. *Journal of*  
19 *Geophysical Research: Space Physics*, 112(A6), 2007.
- 20 Ding, F., Wan, W., Liu, L., Afraimovich, E. L., Voeykov, S. V., and Perevalova, N. P.: A statistical  
21 study of large-scale traveling ionospheric disturbances observed by GPS TEC during major  
22 magnetic storms over the years 2003–2005. *Journal of Geophysical Research: Space*  
23 *Physics*, 113(A3), 2008.
- 24 Ding, F., Wan, W., Ning, B., Zhao, B., Li, Q., Zhang, R., Xiong, B., and Song, Q.: Two-dimensional  
25 imaging of large-scale traveling ionospheric disturbances over China based on GPS  
26 data. *Journal of Geophysical Research: Space Physics*, 117(A8), 2012.
- 27 Ding, F., Wan, W., Ning, B., Zhao, B., Li, Q., Wang, Y., Hu, L., Zhang, R., and Xiong, B.:  
28 Observations of poleward-propagating large-scale traveling ionospheric disturbances in  
29 southern China. In *Annales Geophysicae* (Vol. 31, No. 2, p. 377). Copernicus GmbH, 2013.
- 30 Ding, F., Wan, W., Li, Q., Zhang, R., Song, Q., Ning, B., Liu, L., Zhao, B., and Xiong, B.:  
31 Comparative climatological study of large-scale traveling ionospheric disturbances over North  
32 America and China in 2011–2012. *Journal of Geophysical Research: Space Physics*, 119(1),  
33 519-529, 2014.
- 34 Figueiredo, C. A. O. B., Wrasse, C. M., Takahashi, H., Otsuka, Y., Shiokawa, K., and Barros, D.:  
35 Large-scale traveling ionospheric disturbances observed by GPS dTEC maps over North and  
36 South America on Saint Patrick's Day storm in 2015. *Journal of Geophysical Research: Space*  
37 *Physics*, 122(4), 4755-4763, 2017.
- 38 Foster, J. C., Erickson, P. J., Coster, A. J., Thaller, S., Tao, J., Wygant, J. R., and Bonnell, J. W.:  
39 Storm time observations of plasmasphere erosion flux in the magnetosphere and  
40 ionosphere. *Geophysical Research Letters*, 41(3), 762-768, 2014.
- 41 Fuller-Rowell, T. J., Codrescu, M. V., Moffett, R. J., and Quegan, S.: Response of the thermosphere  
42 and ionosphere to geomagnetic storms. *Journal of Geophysical Research: Space*  
43 *Physics*, 99(A3), 3893-3914, 1994.
- 44 Habarulema, J. B., Katamzi, Z. T., and Yizengaw, E.: First observations of poleward large-scale



- 1 traveling ionospheric disturbances over the African sector during geomagnetic storm  
2 conditions. *Journal of Geophysical Research: Space Physics*, 120(8), 6914-6929, 2015.
- 3 Habarulema, J. B., Katamzi, Z. T., Yizengaw, E., Yamazaki, Y., and Seemala, G.: Simultaneous  
4 storm time equatorward and poleward large-scale TIDs on a global scale. *Geophysical  
5 Research Letters*, 43(13), 6678-6686, 2016.
- 6 Hines, C. O.: Internal atmospheric gravity waves at ionospheric heights. *Canadian Journal of  
7 Physics*, 38(11), 1441-1481, 1960.
- 8 Ho, C. M., Mannucci, A. J., Lindqwister, U. J., Pi, X., and Tsurutani, B. T.: Global ionosphere  
9 perturbations monitored by the worldwide GPS network. *Geophysical Research  
10 Letters*, 23(22), 3219-3222, 1996.
- 11 Hocke, K. and Schlegel, K.: A review of atmospheric gravity waves and travelling ionospheric  
12 disturbances: 1982-1995. In *Annales Geophysicae* (Vol. 14, No. 9, p. 917), 1996.
- 13 Hunsucker, R. D.: Atmospheric gravity waves generated in the high-latitude ionosphere: A  
14 review. *Reviews of Geophysics*, 20(2), 293-315, 1982.
- 15 Jakowski, N., Mielich, J., Borries, C., Cander, L., Krankowski, A., Nava, B., and Stankov, S. M.:  
16 Large-scale ionospheric gradients over Europe observed in October 2003. *Journal of  
17 Atmospheric and Solar-Terrestrial Physics*, 70(15), 1894-1903, 2008.
- 18 Klausner, V., Fagundes, P. R., Sahai, Y., Wrasse, C. M., Pillat, V. G., and Becker-Guedes, F.:  
19 Observations of GW/TID oscillations in the F2 layer at low latitude during high and low solar  
20 activity, geomagnetic quiet and disturbed periods. *Journal of Geophysical Research: Space  
21 Physics*, 114(A2), 2009.
- 22 Klobuchar, J. A.: Design and characteristics of the GPS ionospheric time delay algorithm for single  
23 frequency users. In *PLANS'86-Position Location and Navigation Symposium* (pp. 280-286),  
24 1986.
- 25 Lanyi, G. E. and Roth, T.: A comparison of mapped and measured total ionospheric electron content  
26 using global positioning system and beacon satellite observations. *Radio Science*, 23(4), 483-  
27 492, 1988.
- 28 Lyons, L. R., Nishimura, Y., Zhang, S. R., Coster, A. J., Bhatt, A., Kendall, E., and Deng, Y.:  
29 Identification of Auroral Zone Activity Driving Large-Scale Traveling Ionospheric  
30 Disturbances. *Journal of Geophysical Research: Space Physics*, 124(1), 700-714, 2019.
- 31 Maeda, S. and Handa, S.: Transmission of large-scale TIDs in the ionospheric F2-region. *Journal of  
32 Atmospheric and Terrestrial Physics*, 42(9-10), 853-859, 1980.
- 33 Mendillo, M. and Narvaez, C.: Ionospheric storms at geophysically-equivalent sites—Part 1: Storm-  
34 time patterns for sub-auroral ionospheres. In *Annales Geophysicae* (Vol. 27, No. 4, pp. 1679-  
35 1694). Copernicus GmbH, 2009.
- 36 Morton, F. W. and Essex, E. A.: Gravity wave observations at a southern hemisphere mid-latitude  
37 station using the total electron content technique. *Journal of Atmospheric and Terrestrial  
38 Physics*, 40(10-11), 1113-1122, 1978.
- 39 Nicolls, M. J., Kelley, M. C., Coster, A. J., González, S. A., and Makela, J. J.: Imaging the structure  
40 of a large-scale TID using ISR and TEC data. *Geophysical Research Letters*, 31(9), 2004.
- 41 Pederick, L. H., Cervera, M. A., and Harris, T. J.: Interpreting observations of large-scale traveling  
42 ionospheric disturbances by ionospheric sounders. *Journal of Geophysical Research: Space  
43 Physics*, 122(12), 2017.
- 44 Richmond, A. D. and Roble, R. G.: Dynamic effects of aurora-generated gravity waves on the mid-



- 1 latitude ionosphere. *Journal of Atmospheric and Terrestrial Physics*, 41(7-8), 841-852, 1979.
- 2 Rideout, W. and Coster, A.: Automated GPS processing for global total electron content data. *GPS*  
3 *Solutions*, 10(3), 219-228, 2006.
- 4 Saito, A., Fukao, S., and Miyazaki, S.: High resolution mapping of TEC perturbations with the GSI  
5 GPS network over Japan. *Geophysical research letters*, 25(16), 3079-3082, 1998.
- 6 Saito, A., Nishimura, M., Yamamoto, M., Fukao, S., Kubota, M., Shiokawa, K., Otsuka, Y., Tsugawa,  
7 T., Ogawa, T., Ishii, M., Sakanoi, and T., Miyazaki, S.: Traveling ionospheric disturbances  
8 detected in the FRONT campaign. *Geophysical Research Letters*, 28(4), 689-692, 2001.
- 9 Shiokawa, K., Otsuka, Y., Ogawa, T., Balan, N., Igarashi, K., Ridley, A. J., Knipp, D. J., Saito, A.,  
10 and Yumoto, K.: A large-scale traveling ionospheric disturbance during the magnetic storm of  
11 15 September 1999. *Journal of Geophysical Research: Space Physics*, 107(A6), SIA-5, 2002.
- 12 Song, Q., Ding, F., Wan, W., Ning, B., Liu, L., Zhao, B., Li, Q., and Zhang, R.: Statistical study of  
13 large-scale traveling ionospheric disturbances generated by the solar terminator over  
14 China. *Journal of Geophysical Research: Space Physics*, 118(7), 4583-4593, 2013.
- 15 Thomas, E. G., Baker, J. B. H., Ruohoniemi, J. M., Coster, A. J., and Zhang, S. R.: The geomagnetic  
16 storm time response of GPS total electron content in the North American sector. *Journal of*  
17 *Geophysical Research: Space Physics*, 121(2), 1744-1759, 2016.
- 18 Tsugawa, T., Saito, A., Otsuka, Y., and Yamamoto, M.: Damping of large-scale traveling ionospheric  
19 disturbances detected with GPS networks during the geomagnetic storm. *Journal of*  
20 *Geophysical Research: Space Physics*, 108(A3), 2003.
- 21 Tsugawa, T., Saito, A., and Otsuka, Y.: A statistical study of large-scale traveling ionospheric  
22 disturbances using the GPS network in Japan. *Journal of Geophysical Research: Space*  
23 *Physics*, 109(A6), 2004.
- 24 Tsugawa, T., Shiokawa, K., Otsuka, Y., Ogawa, T., Saito, A., and Nishioka, M.: Geomagnetic  
25 conjugate observations of large-scale traveling ionospheric disturbances using GPS networks  
26 in Japan and Australia. *Journal of Geophysical Research: Space Physics*, 111(A2), 2006.
- 27 Wan, W., Ning, B., Yuan, H., Li, J., Li, L., and Liang, J.: TID observation using a short baseline  
28 network of GPS receivers. *Acta Geodaetica et Geophysica Hungarica*, 32(3-4), 321-327, 1997.
- 29 Wang, C.: New Chains of Space Weather Monitoring Stations in China, *Space*  
30 *Weather*, 8, S08001, doi:10.1029/2010SW000603, 2010.
- 31 Zakharenkova, I., Astafyeva, E., and Cherniak, I.: GPS and GLONASS observations of large-scale  
32 traveling ionospheric disturbances during the 2015 St. Patrick's Day storm. *Journal of*  
33 *Geophysical Research: Space Physics*, 121(12), 2016.
- 34 Zhang, D. H. and Xiao, Z.: Study of ionospheric response to the 4B flare on 28 October 2003 using  
35 International GPS Service network data. *Journal of Geophysical Research: Space*  
36 *Physics*, 110(A3), 2005.
- 37 Zhang, D. H., Zhang, W., Li, Q., Shi, L. Q., Hao, Y. Q., and Xiao, Z.: Accuracy analysis of the GPS  
38 instrumental bias estimated from observations in middle and low latitudes. In *Annales*  
39 *Geophysicae* (Vol. 28, No. 8, pp. 1571-1580). Copernicus GmbH, 2010.
- 40 Zhang, S. R., Foster, J. C., Coster, A. J., and Erickson, P. J.: East-West Coast differences in total  
41 electron content over the continental US. *Geophysical Research Letters*, 38(19), 2011.
- 42 Zhang, S. R., Erickson, P. J., Goncharenko, L. P., Coster, A. J., Rideout, W., and Vierinen, J.:  
43 Ionospheric bow waves and perturbations induced by the 21 August 2017 solar  
44 eclipse. *Geophysical Research Letters*, 44(24), 12-067, 2017.



- 1 Zhang, W., Zhang, D. H., and Xiao, Z.: The influence of geo-magnetic storms on the estimation of
- 2 GPS instrumental biases, Ann. Geophys., 27, 1613-1623, doi:10.5194/angeo-27-1613-2009,
- 3 2009.
- 4



1 **Captions of Table and Figures**

2 **Table 1.** The estimated propagation parameters of the LSTID and the corresponding standard errors.  
3 The second column contains the propagation directions, which are measured clockwise from the  
4 South.  $V_t/V_c$  represents the phase speed estimated with certain wave trough/crest.

5  
6 **Figure 1.** Locations of the GPS stations of different networks (colored dots), the HF Doppler shift  
7 stations (lime stars), the National Time Service Center of China (grey stars), and the ionosondes  
8 (lime triangles) that used in this study.

9  
10 **Figure 2.** Temporal variations of (a) the solar wind speed ( $V_{sw}$ ), (b) the IMF  $B_z$  component, (c) the  
11 SYM-H index, and (d) the AE index between 18:00 UT, 16 March 2015 and 06:00 UT, 18 March  
12 2015. The occurrence of SSC is shown with vertical dashed lines.

13  
14 **Figure 3.** Temporal variations of the HF Doppler shift records from (a) MDT and (b) SZT between  
15 08:00 UT and 14:00 UT, 17 March 2015.

16  
17 **Figure 4.** A series of 2D VTECP' maps over the East Asian sector from the period of 09:40-09:50  
18 UT to 11:30-11:40 UT on 17 March 2015. The grey areas represent the nightside. The colorbar  
19 represents the VTECP' (units: TECu). The lime and yellow lines illustrate the least square fittings  
20 (order 2) for wavefronts.

21  
22 **Figure 5.** Temporal variations of mean VTECP' near the Doppler reflection points between 08:00  
23 UT and 14:00 UT, 17 March 2015.

24  
25 **Figure 6.** Temporal variations of the virtual height for iso-frequency lines from 8 ionosondes  
26 between 08:00 UT and 12:00 UT, 17 March 2015. Frequencies are depicted on each iso-frequency  
27 line. The time resolution is 15 min for all stations. The red dashed lines connect the peaks of the  
28 highest and lowest frequencies.

29  
30 **Figure 7.** A detailed example of the wavefront fitting method. Lime dots indicate the data points for  
31 least square fitting. Lime arrows depict the propagation orientations in different longitudes. Dashed  
32 black rectangles mark the areas for generating TLPs in Figure 8.

33  
34 **Figure 8.** TLPs of VTECP' for different longitudinal bands between 07:00-14:00 UT. White dots  
35 give the data points for linear fitting, and the fitting results are marked with white lines. Black  
36 dashed lines depict 30°N in (b-d, f) and 40°N in (f).

37  
38 **Figure 9.** The sketch of (upper) the geomagnetic declination angels and (lower) the propagation  
39 directions in different longitudes on the wavefront fitted in Figure 7. The propagation directions are  
40 measured clockwise from the South.

41  
42 **Figure 10.** The TLP of VTECP' for the European sector (10°E-20°E, 30°N-70°N) between 01:00-  
43 23:00 UT. White lines and dots are similar to those in Figure 8. The black dashed line depicts 60°N.

44



1 **Table 1.**

Lon. (°E)	Dir. (°)	Period (min)	Vt (m/s)	Vc (m/s)	Wavelength (km)
80-90	-11.2	81.1 ± 3.4	500 ± 40	542 ± 31	2536 ± 163
90-100	-7.1	77.6 ± 5.2	552 ± 22	670 ± 44	2845 ± 222
100-110	-2.9	58.8 ± 1.5	587 ± 47	638 ± 76	2160 ± 167
110-120	1.3	62.4 ± 2.0	605 ± 27	562 ± 25	2184 ± 99
120-130	7.9	94.2 ± 1.3	647 ± 39	673 ± 63	3731 ± 216

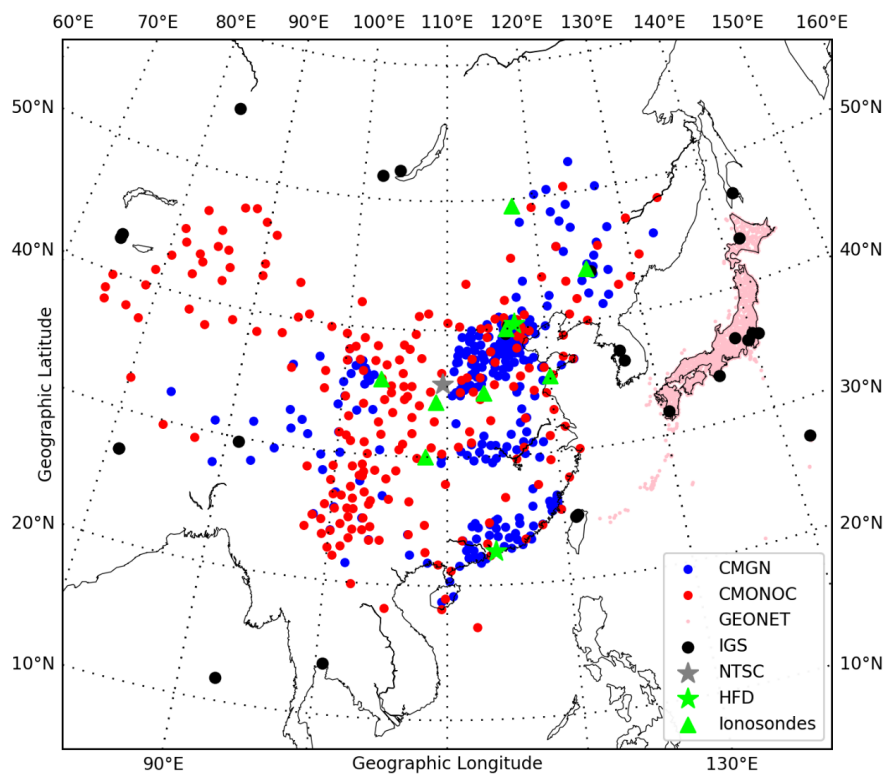
2

3





1 Figure 1.

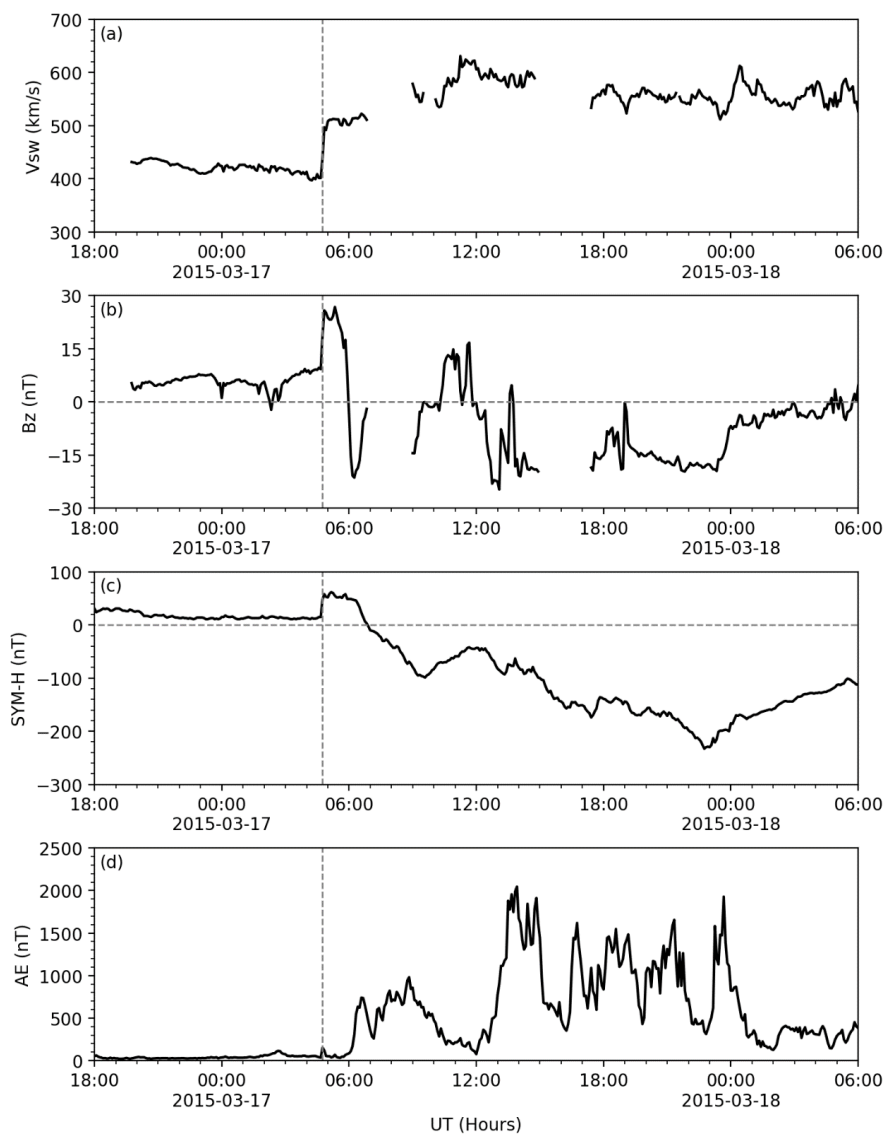


2

3



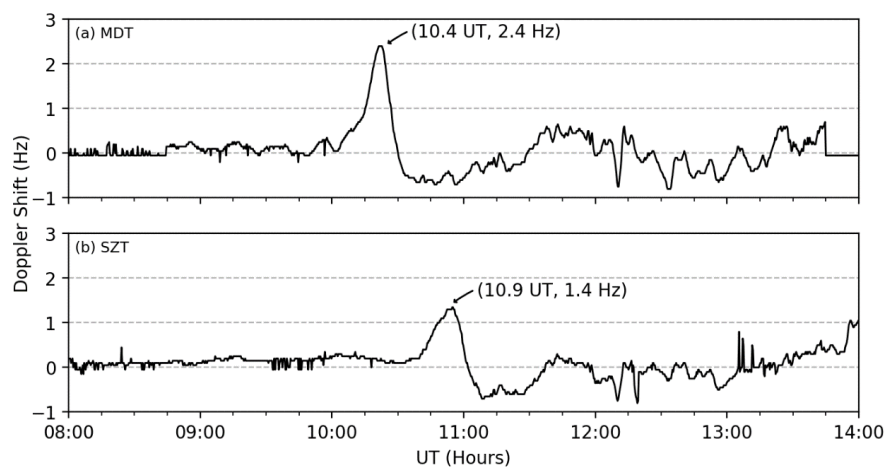
1 Figure 2.



2  
3  
4



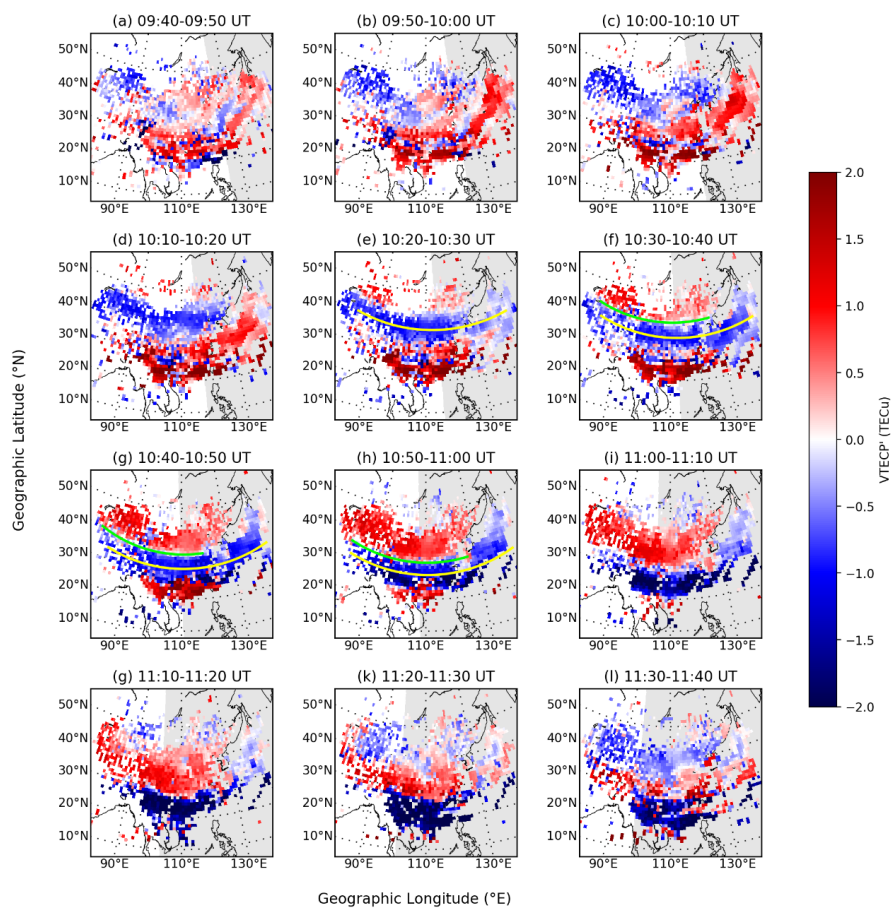
1 Figure 3.



2  
3  
4



1 Figure 4.



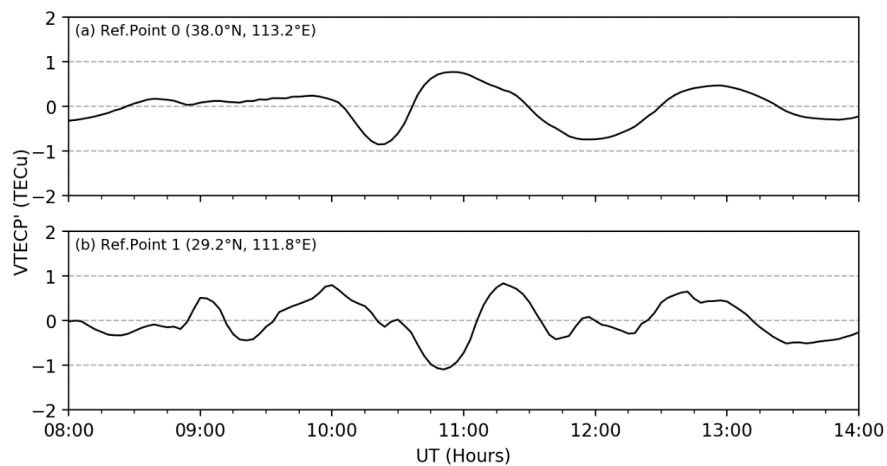
2

3

4



1 Figure 5.

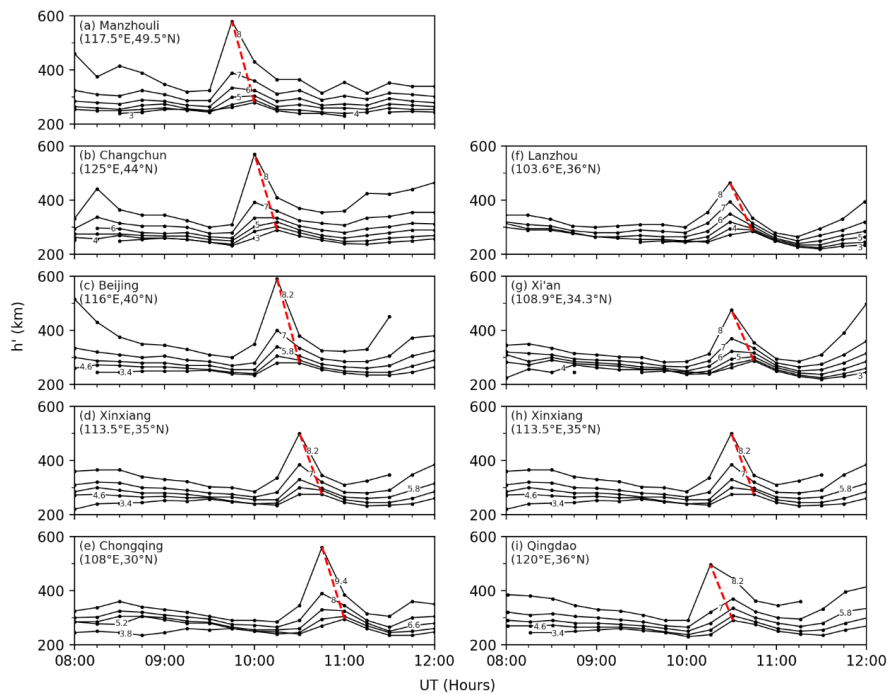


2

3



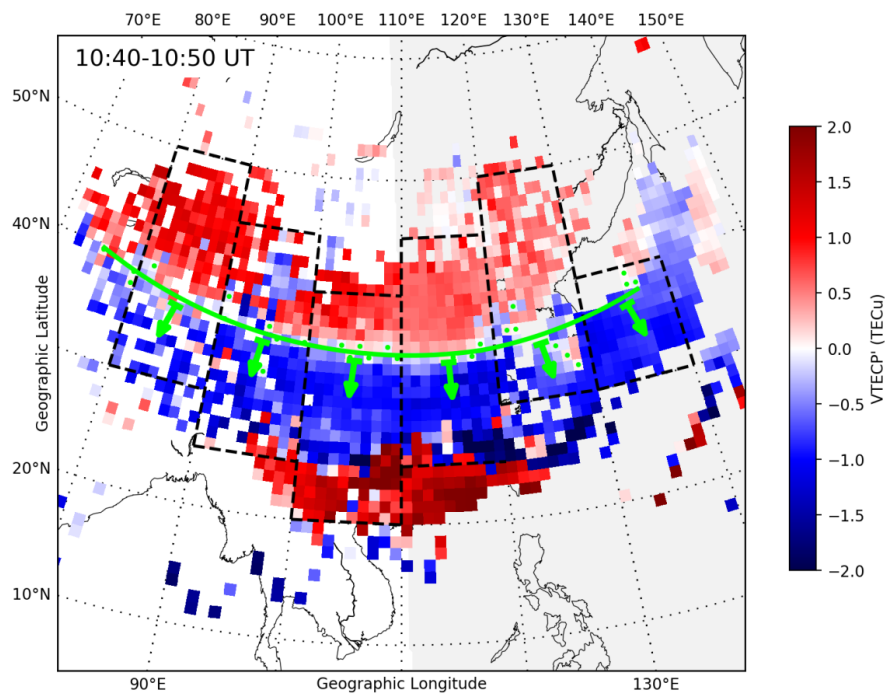
1 Figure 6.



2  
3



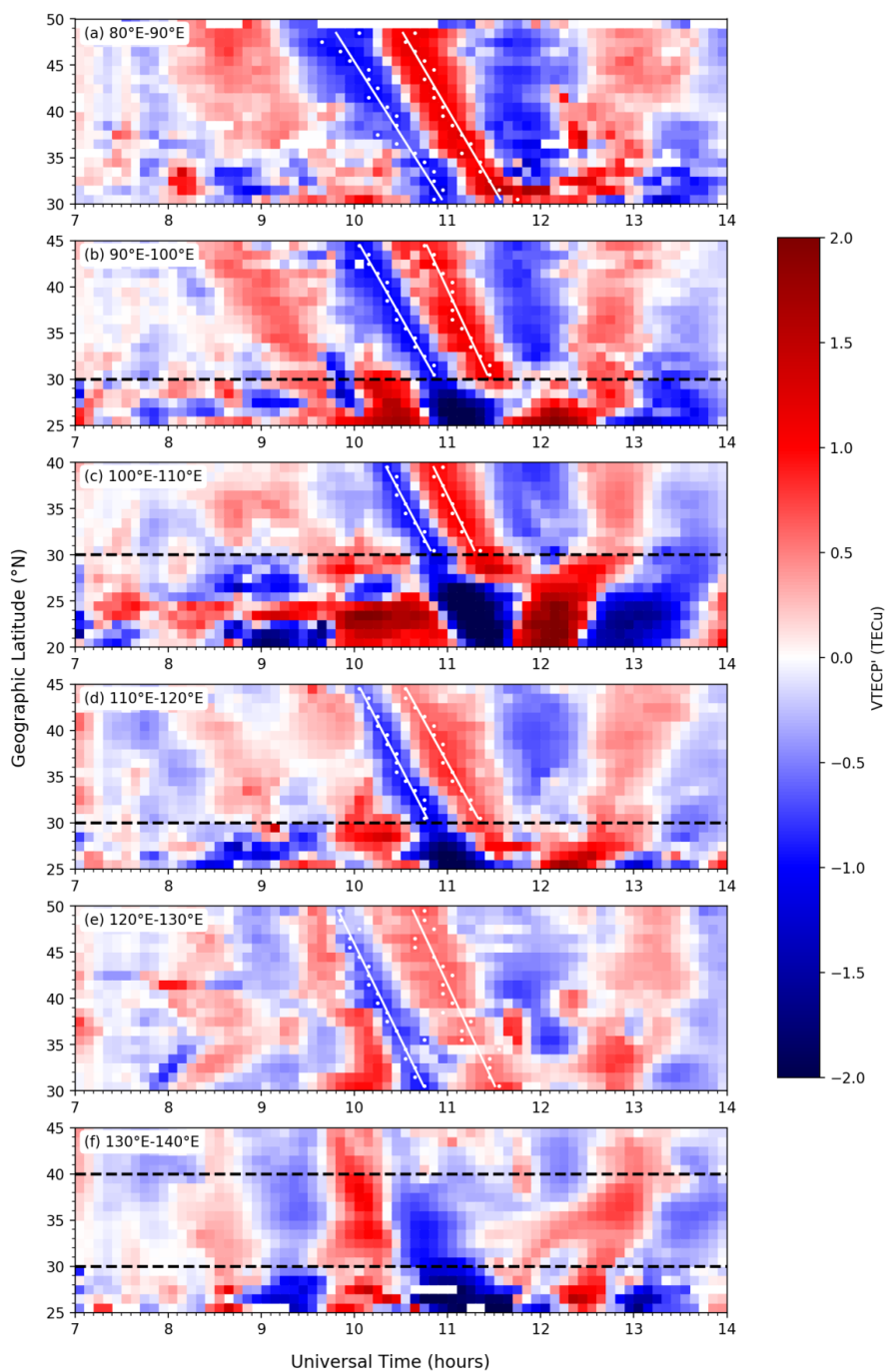
1 Figure 7.



2  
3  
4



1 Figure 8.



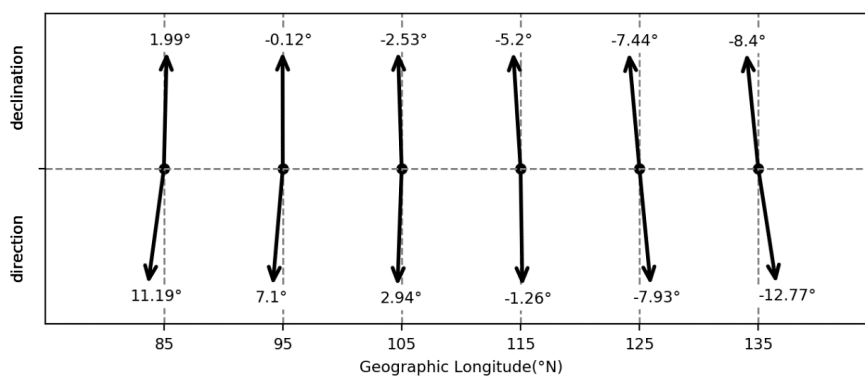
2

3





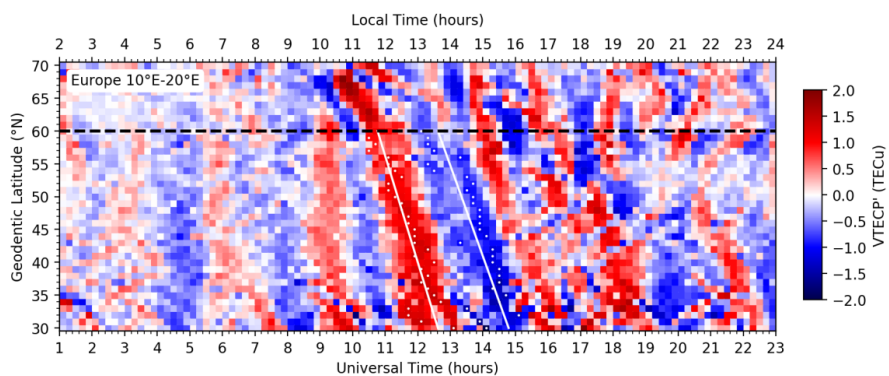
1 Figure 9.



2  
3  
4



1 Figure 10.



2

3